

STATISTICAL STUDIES BASED ON SIMULTANEOUS SiO AND H₂O MASER SURVEYS TOWARD EVOLVED STARS

JAEHEON KIM¹, SE-HYUNG CHO^{1,2}, AND SANG JOON KIM³

¹ Advanced Astronomy and Space Science Division, Korea Astronomy and Space Science Institute, 776, Daedeokdae-ro, Yuseong-gu, Daejeon 305-348, Korea; jhkim@kasi.re.kr, cho@kasi.re.kr

² Department of Astronomy, Yonsei University, Seongsan-ro 262, Seodaemun, Seoul 120-749, Korea

³ Department of Astronomy and Space Science, Kyung Hee University, Seocheon-Dong, Giheung-Gu, Yongin, Gyeonggi-Do 446-701, Korea; sjkim1@khu.ac.kr

Received 2013 May 15; accepted 2013 October 29; published 2013 December 12

ABSTRACT

Based on the simultaneous observational results of SiO and H₂O masers toward 401 evolved stars, we have performed statistical analyses. We find that the peak and integrated intensities of SiO masers are stronger than those of H₂O masers in both Mira variables and OH/IR stars at most optical phases. However, the relative intensity ratios of H₂O to SiO masers in OH/IR stars are larger than those in Mira variables. Moreover, the intensity ratios of H₂O to SiO masers are found to be increased around the optical phases from 0–0.4. The H₂O photon luminosities also tend to be more dependent on the optical phase compared with those of SiO masers. These facts suggest that H₂O masers are more sensitive to expanding the motion of circumstellar envelopes and also shock waves arising from the pulsations of the central star compared with SiO masers. This result may also be related to the differences in the maser location and pumping mechanism between H₂O and SiO masers. The full width at zero power of SiO masers in Mira variables shows similar values to those of OH/IR stars, while those of H₂O masers in OH/IR stars show larger values than those of Mira variables. These differences may originate from the different mass-loss rates and the different location of the two masers. The mean velocity shift of SiO and H₂O masers with respect to the stellar velocity was investigated as a function of optical phase. The velocity shift of the H₂O masers shows that the redshifted emission dominates during the phases from 0.3–0.6, while the blueshifted emission appears at phase 0.6 and coexists with the redshifted emission during other phases. These features show an associated pattern with the CO $\Delta V = 3$ radial velocity curve, which exhibits a typical pulsation motion. On the other hand, the velocity shift of the SiO $v = 2$ maser shows slightly similar features to the H₂O maser, while that of SiO $v = 1$ does not show these similar features. Finally, the distributions of all 401 observed sources are investigated in the *IRAS* two-color diagram in relation to the late evolutionary processes of asymptotic giant branch stars.

Key words: circumstellar matter – masers – radio lines: stars – stars: late-type

Online-only material: machine-readable and VO tables

1. INTRODUCTION

Most late-type stars with main sequence masses of 1–8 M_{\odot} evolve from the asymptotic giant branch (AGB) to the planetary nebula (PN) phase. They lose a significant fraction of their initial mass through pulsation-driven mass loss (Vassiliadis & Wood 1993). As a representative type of AGB star, Mira variables are long-period pulsating variable stars characterized by very red colors and regular pulsation periods of ~ 200 –800 days. Material escapes into space in the form of a strong stellar wind at a rate of $\sim 10^{-8}$ – $10^{-6} M_{\odot} \text{ yr}^{-1}$ and envelope expansion velocities of 5–10 km s^{-1} . As another representative member of AGB stars, OH/IR stars have higher masses (3–8 M_{\odot}) than Mira variables. They also show thicker circumstellar envelopes (CSEs), higher mass-loss rates (10^{-7} to $10^{-4} M_{\odot} \text{ yr}^{-1}$), longer pulsation periods (300–3000 days), and higher expansion velocities (5–30 km s^{-1}) compared with Mira variables.

It is well known that these AGB stars emit SiO, H₂O, and OH masers from their different shells according to chemical and excitation conditions (Reid & Moran 1981). The SiO maser emission occurs at the region close to a central star where turbulent motion and acceleration are important, whereas the 22 GHz H₂O maser arises from above the dust-forming layer where circumstellar gas is expanding. A large number of AGB stars show SiO masers together with H₂O masers. However, systematic

studies on the mutual relations between SiO and H₂O masers have not been performed yet for sources in which both SiO and H₂O masers are detected due to the lack of homogeneous data obtained from simultaneous observations of SiO and H₂O masers using the same telescope system. Recently, simultaneous survey and monitoring observations of SiO and 22 GHz H₂O masers using the Korean VLBI Network (KVN) single dishes were carried out by Kim et al. (2010, hereafter Paper I), Cho & Kim (2012, hereafter Paper II), Kim et al. (2013, hereafter Paper III), and S. H. Cho et al. (2014, in preparation). These homogeneous data enable us to perform a combined study of SiO and H₂O masers toward SiO and/or H₂O maser sources through statistical analyses. Statistical studies are useful and provide insight into the complex and varied phenomena in maser emission associated with stellar pulsation. In particular, AGB stars show very long periods from about 150–1000 days. Previous statistical studies of SiO maser emission were carried out by Spencer et al. (1981), Jewell et al. (1991), and Cho et al. (1996). From their studies, clear correlations were shown between SiO maser emission and the optical phase of the central star. For example, the SiO $v = 1$, 2, $J = 1-0$ masers show their flux maxima near an optical phase of 0.2, which is consistent with the results of long-term time monitoring observations of individual stars (Alcolea et al. 1999; Pardo et al. 2004). Moreover, the behavior of the mean

Table 1
Type of Evolved Stars and a Summary of the Observational Results

Type of Object	Sources Surveyed	Sources Both Detected	Sources SiO-only Detected	Sources H ₂ O-only Detected	Sources Both Undetected
Mira variable	214	112	78	3	21
OH/IR star	73	32	29	3	9
Semi-regular variable	52	21	6	11	14
Infrared source	19	9	3	5	2
Irregular variable	11	3	1	1	6
Supergiant	10	8	2
Carbon star	10	3	7
OH maser source	5	1	3	...	1
Post-AGB star	5	1	1	1	2
S star	2	1	1
Total	401	188	124	27	62

velocity as a function of optical phases shows a meaningful feature associated with stellar pulsation (Cho et al. 1996). In addition, Benson & Little-Marenin (1990) and Little-Marenin & Benson (1991) found that the intensity of the H₂O maser emission is highly variable and often changes in the phase with the optical light curve, typically showing a phase lag of about 0.1–0.4 phases with respect to the optical maximum. Similarly, long-term monitoring of 22 GHz H₂O maser emission has been made by Lekht et al. (2005, and references therein) for various semi-regular variables, Mira variables, and supergiants. For the sources with large-amplitude variations, they also found that the integrated H₂O maser emission is correlated with the optical emission of the star with phase lags of 0.01–0.5. Shintani et al. (2008) performed statistical analyses to elucidate the physical properties of H₂O maser gas clumps and accompanying CSEs toward the samples of H₂O maser and stellar optical emission for 46 AGB stars. They found a correlation between the time lag of the H₂O maser flux variation with respect to the optical magnitude variation and the stellar pulsation period, leading to a limited phase lag range of 0.7–1.5. Moreover, Engels et al. (1986) confirmed that the H₂O maser luminosity of OH/IR stars also follows the cycle of variation of the infrared and OH luminosities with a phase lag of 0.2.

In addition, recent multi-epoch Very Long Baseline Array observations of SiO masers (Diamond & Kemball 2003; Yi et al. 2005; Gonidakis et al. 2010) have shown that the diameter of the synthetic maser ring is dependent on stellar phase and maser transition, broadly consistent with the model of Humphreys et al. (2002). A periodic variation in the angular distribution of H₂O maser features was also reported (Bowers & Johnston 1994). They strongly suggest that the pulsation of the central star causes oscillations in this portion of the envelope, with shock waves propagating outward and with material falling inward. Therefore, combined studies of SiO and H₂O maser emission through statistical analyses also provide a useful probe of the spatial structure and kinematics of CSEs and the mass-loss process in AGB stars including the characteristics related to the evolutionary stage of AGB stars.

Sample sources and data sets are given in Section 2 and statistical analyses based on our homogeneous data are presented in Section 3. In Section 4, we present a summary and conclusions.

2. SAMPLE SOURCES AND DATA SETS

The sample stars that we use for our statistical studies are 401 evolved stars in total that were observed with the KVN single dish, as described in Papers I–III. They are mainly

composed of Mira variables, OH/IR stars, and semi-regular variables, as shown in Table 1. Both SiO and H₂O maser lines have been detected above the 3σ level from 47% of the entire source sample. SiO-only maser lines without H₂O maser detections have been detected from 124 sources with a detection rate of 31%, while H₂O-only maser lines without SiO maser detections have been detected from 27 sources, with a detection rate of 7%. We have used the peak and integrated intensities, their ratios, and the mean velocity data of observed SiO $v = 1, 2$, $J = 1-0$ (hereafter, SiO $v = 1, 2$) and H₂O $6_{16} - 5_{23}$ (hereafter, H₂O) maser lines published in Papers I, II, and III. In addition, the full width at zero power (FWZP) and the velocity shift with respect to stellar velocity were measured and the photon luminosity was estimated in order to investigate the correlation between SiO and H₂O masers and stellar pulsation.

The data used in the analyses are given in Tables 2 and 3. In Table 2, the identification number of Papers I–III and the source name are given in Columns 1 and 2. In Column 1, the Roman numerals in parentheses represent Papers I–III, respectively. Columns 3–5 list the integrated flux for SiO $v = 1, 2$, and H₂O maser lines as a unit of W m^{-2} and Columns 6–8 list the calculated photon luminosities of each maser on a log scale in units of photons s^{-1} . Column 9 lists the phase of the optical light curve at the epoch of the observation, calculated from the optical data provided by the American Association of Variable Star Observers (AAVSO) and the All Sky Automated Survey of Pojmanski (2002). The optical phases are available for 161 out of 401 sources. We have listed the distance to sources found in the literature in Column 10. Table 3 gives the FWZPs, i.e., velocity ranges between the limits of the blue and red line edges where the maser emission decreased to the noise level, of the SiO $v = 1, 2$ and H₂O maser lines and the ratios of H₂O to SiO $v = 1$ maser lines. In Columns 7–9, the mean velocity, i.e., the same meaning as the velocity centroid of McIntosh (2006), with respect to the stellar velocity, $V_{\text{mean}} - V^*$, is given. Both SiO and H₂O undetected sources are not listed in all tables.

3. STATISTICAL ANALYSES

As discussed in Section 1, previous statistical studies based on a statistical snapshot at a single phase of many sources are very useful and provide conclusions (e.g., Spencer et al. 1981; Jewell et al. 1991; Cho et al. 1996) consistent with time monitoring observations of individual sources (Alcolea et al. 1999; Pardo et al. 2004). However, there are some limitations to these statistical analyses because the individual sources have different strengths, distances, periods, etc., and may not be

Table 2
Photon Luminosity of Detected Sources

No.	Source	Integrated Flux ($\times 10^{-20}$ W m $^{-2}$)			log(Pho. Lum.) (photons s $^{-1}$)			Phase	Distance
		SiO $v = 1$	SiO $v = 2$	H $_2$ O	SiO $v = 1$	SiO $v = 2$	H $_2$ O		
(1)	(2)	(3)	(4)	(5)	(6)	(7)	(8)	(9)	(10)
1(I)	Y Cas	40.45	34.44	2.94	44.03	43.97	43.18	0.25	798.00 ⁽³⁾
2(I)	SY Scl	0.78	3.17	1.35	0.22	...
3(I)	S Scl	3.03	3.24	...	42.22	42.25	...	0.42	362.00 ⁽³⁾
4(I)	R And	1.53	42.49	0.79	692.00 ⁽³⁾
5(I)	V524 Cas	13.57	10.81	2.81
6(I)	WX Psc	44.09	52.19	15.17	44.00	44.08	43.83	0.13	740.00 ⁽¹⁶⁾
7(I)	V669 Cas	0.92	3.03	...	42.91	43.44	1460.00 ⁽²²⁾
8(I)	V370 And	0.85	41.01	170.34 ⁽¹⁾
9(I)	W And	8.27	3.42	...	42.92	42.54	...	0.89	490.00 ⁽⁵⁾
10(I)	σ Cet	17.04	59.58	0.46	42.05	42.60	41.77	0.49	125.53 ⁽¹⁾

References. (1) Anderson & Francis 2012; (2) Deguchi et al. 2012; (3) Pickles & Depagne 2010; (4) Choi et al. 2008; (5) Whitelock et al. 2008; (6) Imai et al. 2007; (7) Nakashima & Deguchi 2007; (8) Ammons et al. 2006; (9) Justtanont et al. 2006; (10) Deguchi et al. 2004; (11) Nakashima & Deguchi 2003b; (12) Nakashima & Deguchi 2003a; (13) Le Bertre et al. 2003; (14) van Belle et al. 2002; (15) Ita et al. 2001; (16) Olivier et al. 2001; (17) Nakashima et al. 2000; (18) Hale et al. 1997; (19) van Belle et al. 1996; (20) Benson & Little-Marenin 1996; (21) Izumiura et al. 1995; (22) Loup et al. 1993; (23) Palagi et al. 1993; (24) Nyman et al. 1993; (25) Kastner et al. 1992; (26) Jura & Kleinmann 1989; (27) Bujarrabal et al. 1987; (28) Morris & Jura 1983; (29) Spencer et al. 1981; (30) Engels 1979.

(This table is available in its entirety in machine-readable and Virtual Observatory (VO) forms in the online journal. A portion is shown here for guidance regarding its form and content.)

Table 3
FWZP and Velocity Shift of Detected Sources

No.	Source	FWZP (km s $^{-1}$)			FWZP(H $_2$ O)	$V_{\text{mean}} - V^*$ (km s $^{-1}$)		
		SiO $v = 1$	SiO $v = 2$	H $_2$ O	FWZP(SiO $v = 1$)	SiO $v = 1$	SiO $v = 2$	H $_2$ O
(1)	(2)	(3)	(4)	(5)	(6)	(7)	(8)	(9)
1(I)	Y Cas	15.23	16.37	13.03	0.86	1.8	0.1	-0.9
2(I)	SY Scl	9.56	9.06	4.57	0.48	-2.7	2.1	-1.7
3(I)	S Scl	12.78	12.03	-0.2	-0.4	...
4(I)	R And	5.64	3.2
5(I)	V524 Cas	17.39	13.10	13.95	0.80	3.1	3.6	2.8
6(I)	WX Psc	13.10	11.80	36.55	2.79	-1.9	-1.7	-0.3
7(I)	V669 Cas	10.53	13.57	-2.8	-2.4	...
8(I)	V370 And	11.10	2.0
9(I)	W And	17.43	9.59	-0.4	-0.7	...
10(I)	σ Cet	8.09	5.50	14.72	1.82	3.7	3.4	0.9

(This table is available in its entirety in machine-readable and Virtual Observatory (VO) forms in the online journal. A portion is shown here for guidance regarding its form and content.)

repeatable cycle after cycle. For establishing the validity of the statistical analysis, we include regular variables, i.e., all Mira-type stars and semi-regular variables when periodic behaviors are associated. In addition, the W Hya monitoring results have been compared with statistical results earlier as a validation of the statistical method. In this section, mutual relations between SiO and H $_2$ O maser properties according to stellar pulsation phases and type of evolved stars are investigated on the basis of peak/integrated intensity ratios, photon luminosities, full line widths, and velocity patterns. For all observed sources, we investigate the characteristics of SiO and H $_2$ O maser properties related with evolutionary stages in the *IRAS* two-color diagram.

3.1. Ratios of the Peak and Integrated Intensities of SiO and H $_2$ O Masers

Figure 1 shows the monitoring results of both SiO $v = 1$, 2 and H $_2$ O maser lines that have been simultaneously monitored toward W Hya using the KVN 21m single dish telescope from

2009 June to 2012 May (S.-H. Cho et al. 2014, in preparation). In Figure 1, the peak and integrated intensities of the SiO $v = 1$, 2 and H $_2$ O masers and their ratios of H $_2$ O to SiO $v = 1$ masers are shown as a function of Julian date together with light curves of three stellar periods for W Hya as a representative source. The optical light curve data were obtained by the AAVSO and the vertical blue dashed lines mark the dates of optical maxima. W Hya is a semi-regular variable star with spectral type M7.5e–M9ep and V magnitude 5.5–9.9 (A. A. Henden 2010, private communication). The period of the optical variation of W Hya is approximately 390 days. As shown in Figure 1, the observed points of the SiO and H $_2$ O data are limited except around the second optical maximum between JD 2455200 and 2455400. We could not observe anything during the third and fourth maxima phases due to the system maintenance schedule. However, the peak and integrated intensities of SiO $v = 1$ and $v = 2$ show maxima with a slight time delay with respect to the second optical maximum phase, as was already well known (Martínez et al. 1988; Alcolea et al. 1999), while those of

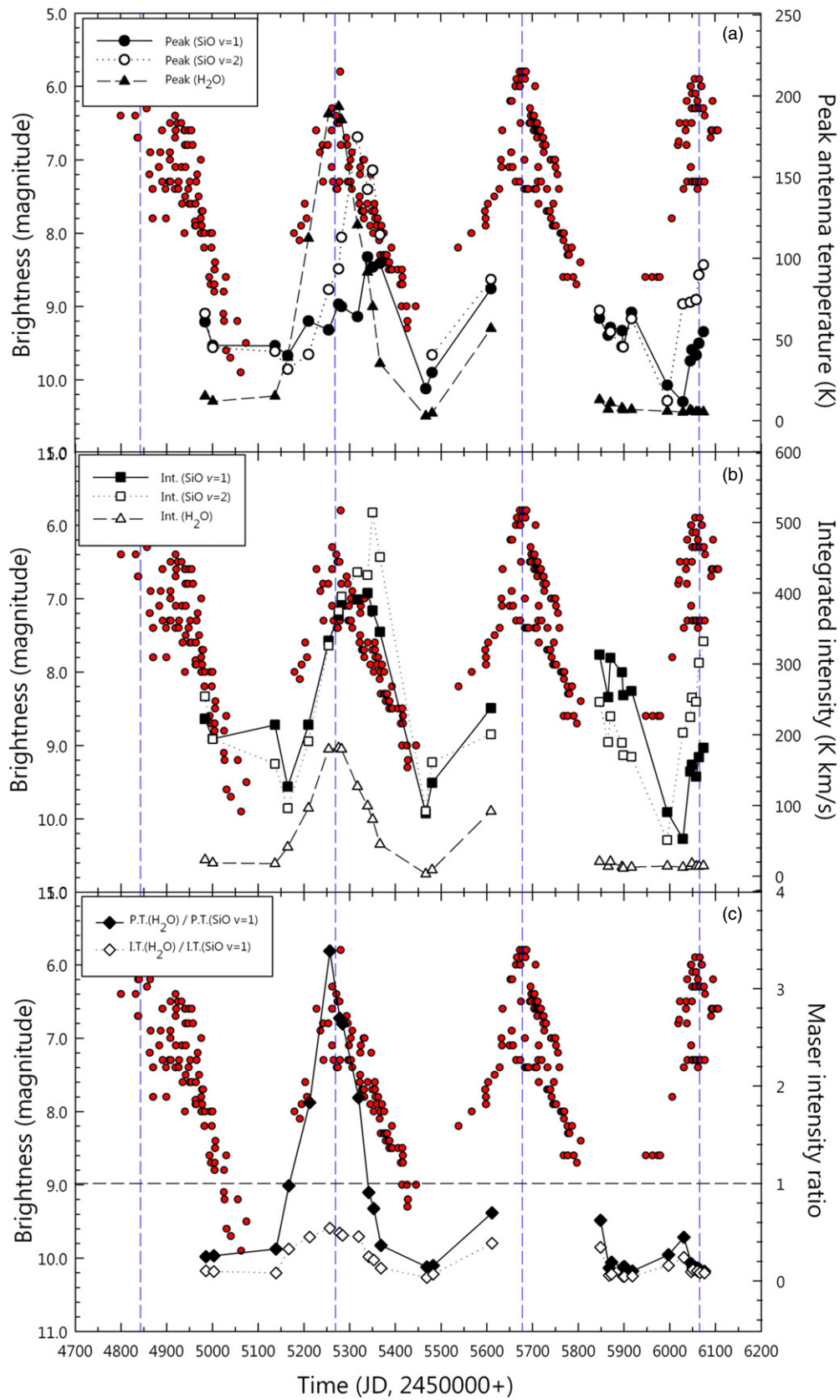


Figure 1. Results of the time monitoring observations of W Hya. Red circles show the optical magnitudes that have been obtained by the AAVSO. Dates of the optical maxima are indicated on 2009 January 11, 2010 March 13, 2011 April 26, and 2012 May 17 by the vertical blue dashed lines. The symbols used are described in the legend inside the plot.

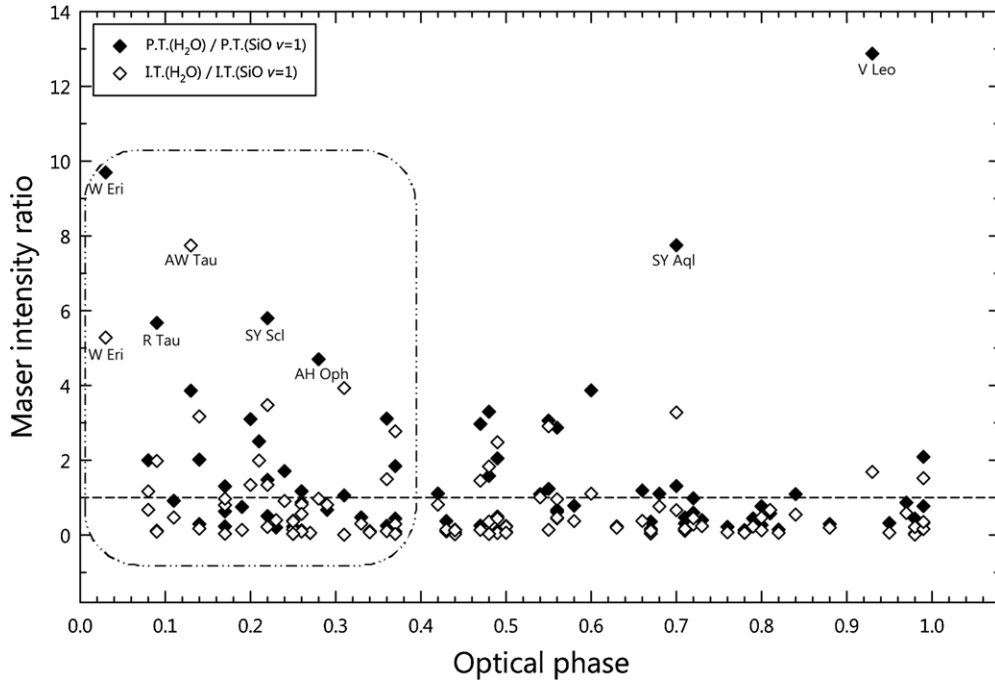


Figure 2. Peak (P.T.) and integrated (I.T.) intensity ratios of the H_2O to $\text{SiO } v = 1$ masers according to the optical phase. The symbols used are described in the legend inside the plot. The dash-dotted area shows the range of phases for the maxima intensity ratios.

H_2O show maxima at the optical maximum phase, as shown in Figures 1(a) and (b). In Figure 1(c), the maxima of the peak and integrated intensity ratios of the H_2O to $\text{SiO } v = 1$ maser are shown at the optical maximum (P.T.(H_2O)/P.T.($\text{SiO } v = 1$) is larger than 3), where “P.T.” refers to the peak antenna temperature. This means that the peak intensity of the H_2O maser rapidly increases around these optical maximum phases compared with that of the SiO maser. This tendency is similar to the results of statistical analyses based on a large sample of sources observed at random stellar phases shown in Figure 2. Namely, a large number of sources with higher values of peak and integrated intensity ratios of the H_2O to $\text{SiO } v = 1$ maser also appear around the optical maximum and the peak intensity of H_2O maser rapidly increases around these optical maximum phases compared with that of SiO maser, as would the time monitoring of W Hya (Figure 1(c)). In addition, the maxima of the SiO and H_2O maser emission occur at phases of about 0.05–0.2 and at phases of about 0.01 in Figures 1(a) and (b), respectively. These results are also consistent with the photon luminosity maxima according to the optical phases based on statistical analyses in Figure 4. On the subject of the rapid increases of H_2O maser peak intensity around optical maximum phases compared with those of SiO masers, one can think that a certain pumping mechanism may be operated around the optical maximum, which causes a stronger peak intensity of H_2O masers as compared with SiO masers. One possibility for this stronger intensity of H_2O masers may be a shock wave effect caused by stellar pulsation. Because H_2O maser is collisionally pumped, while SiO maser is explained by both collisional and radiative pumping, the shock wave effect may be more sensitive to H_2O masers than SiO masers. These results may provide an important clue for different pumping mechanisms and conditions between H_2O and SiO masers in relation to stellar pulsation.

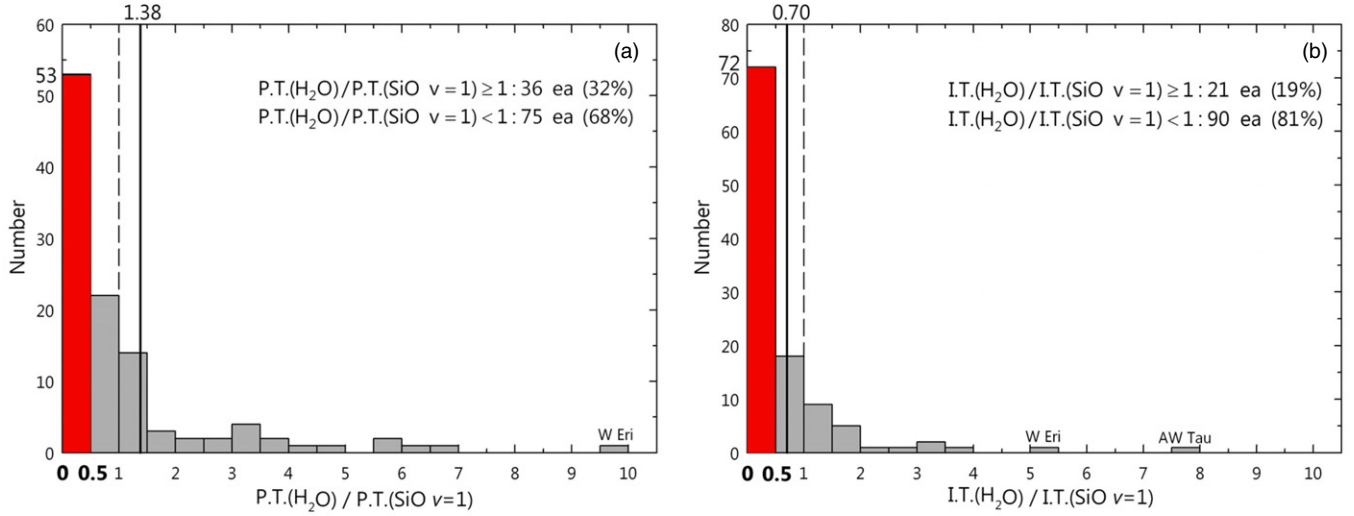
Meanwhile, the maxima of H_2O maser intensities nearly coincide with the optical maxima of the star without a time delay.

This fact cannot be clearly delineated because the H_2O maser emission peaks are not constant but vary from 0.0–2.0 periods (Rudnitskij et al. 1999) and from 0.7–1.5 periods (Shintani et al. 2008). Considering these facts, the phase lags of H_2O maser emission may vary according to sources and cycles, even for the same source.

In Figure 2, the peak and integrated intensity ratios (I.T.) of H_2O to $\text{SiO } v = 1$ maser lines, P.T.(H_2O)/P.T.($\text{SiO } v = 1$) and I.T.(H_2O)/I.T.($\text{SiO } v = 1$), are plotted with respect to the optical phase of a central star in order to investigate any variational pattern related to the stellar pulsation cycle as a statistical treatment for a large number of sources with different optical phases. These ratios are less than 1 in most optical phases. Namely, $\text{SiO } v = 1$ masers emit with a stronger intensity than H_2O masers in most optical phases. However, relatively many sources that have ratios larger than 1 are distributed around the optical phases from 0–0.4 (dash-dotted area), except SY Aql and V Leo. This means that H_2O maser intensity rapidly increases around these optical maximum phases compared with SiO maser intensity.

In Figure 3, we display histograms of the number of stars according to the peak antenna temperature ratios of the H_2O to $\text{SiO } v = 1$ maser lines, P.T.(H_2O)/P.T.($\text{SiO } v = 1$), and integrated intensity ratios of the H_2O to $\text{SiO } v = 1$ maser lines, I.T.(H_2O)/I.T.($\text{SiO } v = 1$), for 111 Mira variables and 32 OH/IR stars, which are both H_2O and SiO maser detected sources. As a whole, SiO maser intensity is stronger than the H_2O maser intensity for both Mira variables and OH/IR stars. Their percentages are indicated in the figure. However, as shown in Figures 3(a) and (b), 53 and 72 sources of 111 Mira variables for the peak and integrated intensity ratios of the H_2O to $\text{SiO } v = 1$ maser line, respectively, are distributed in the ratios between 0–0.5, with ratios of 48% and 65%, respectively, which means a much stronger SiO maser intensity compared with the intensity of H_2O masers for Mira variables. On the other hand, 8 and 10 sources of the 32 OH/IR stars for the peak and integrated intensity

Mira variables



OH/IR stars

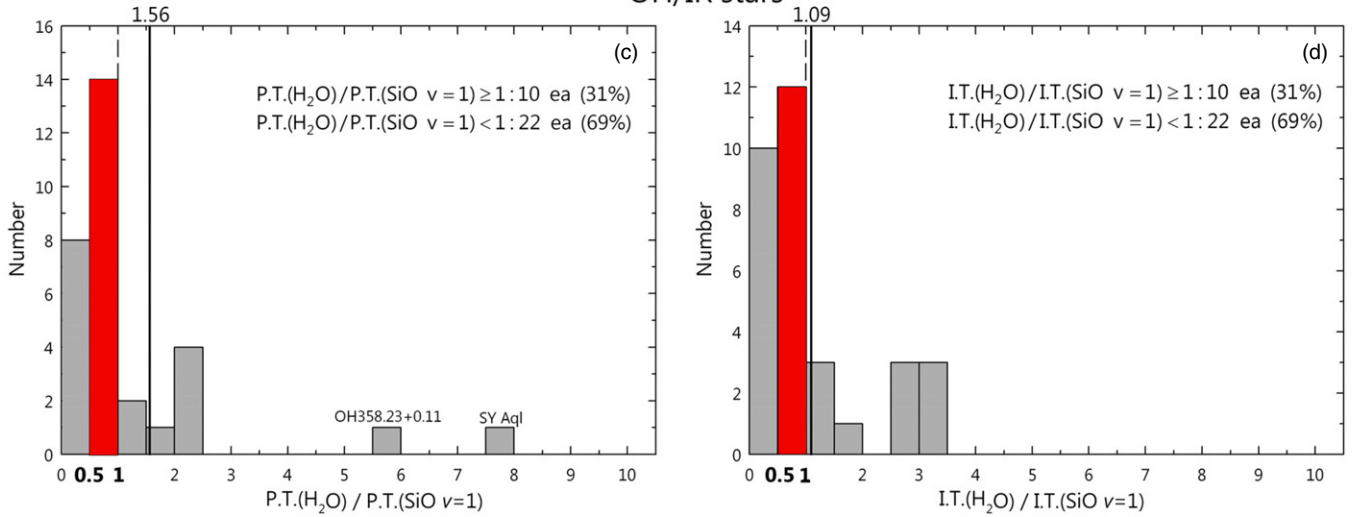


Figure 3. Distribution of the peak (P.T.) and integrated (I.T.) intensity ratios of the H₂O to SiO $\nu = 1$ maser lines for Mira variables ((a) and (b)) and OH/IR stars ((c) and (d)). The dashed line represents a ratio of 1 and the solid line represents the average value of the intensity ratios. The red bin indicates a more dominant range than the others.

ratios are distributed with ratios between 0–0.5, with ratios of 25% and 31%, respectively, while 14 and 12 sources have ratios between 0.5–1.0, respectively, as shown in Figures 3(c) and (d). In addition, the average values of the peak and integrated intensity ratios of the H₂O to SiO $\nu = 1$ maser line for OH/IR stars, 1.56 and 1.09, are large compared with the average values for Mira variables, 1.38 and 0.70. These distributions indicate that the relative intensity ratios of H₂O to SiO maser in OH/IR stars are larger than those in Mira variables, although the intensities of H₂O maser emission are weaker than those of SiO masers in both OH/IR stars and Mira variables. It may be that the H₂O maser photon luminosities of OH/IR stars are larger than those of Mira variables and/or the SiO maser photon luminosities of OH/IR stars are smaller than those of Mira variables. We will discuss this point in detail in Section 3.2.

3.2. Photon Luminosities of SiO and H₂O Masers

By adding the distance information of detected sources, the relationship between SiO and H₂O masers and between Mira variables and OH/IR stars become clearer. From the integrated

intensity and the distance of each detected source, we can estimate the photon luminosity. The integrated flux density (W m^{-2}) can be determined using the following relation

$$S = \int S_\nu d\nu = \frac{2k}{A_e} \int T_A^* d\nu \frac{1}{d\lambda}, \quad (1)$$

where k is Boltzmann's constant and A_e is the effective aperture of the antenna. The photon luminosity (photon s^{-1}) can be estimated as

$$L = \frac{4\pi d^2 S}{h\nu}, \quad (2)$$

where d is the distance to the source, h is Planck's constant, and ν is the observational frequency. In Figure 4, we plot estimated logarithmic photon luminosities of SiO $\nu = 1, 2$ and H₂O masers versus optical phases from Table 2 in order to investigate a stellar optical phase dependence of the photon luminosities in association with Figures 2 and 3. The black circle indicates the photon luminosities of the SiO $\nu = 1$ maser for 125 stars and the red circle indicates the photon luminosities of the SiO $\nu = 2$ maser for 121 stars. The green triangle indicates the photon

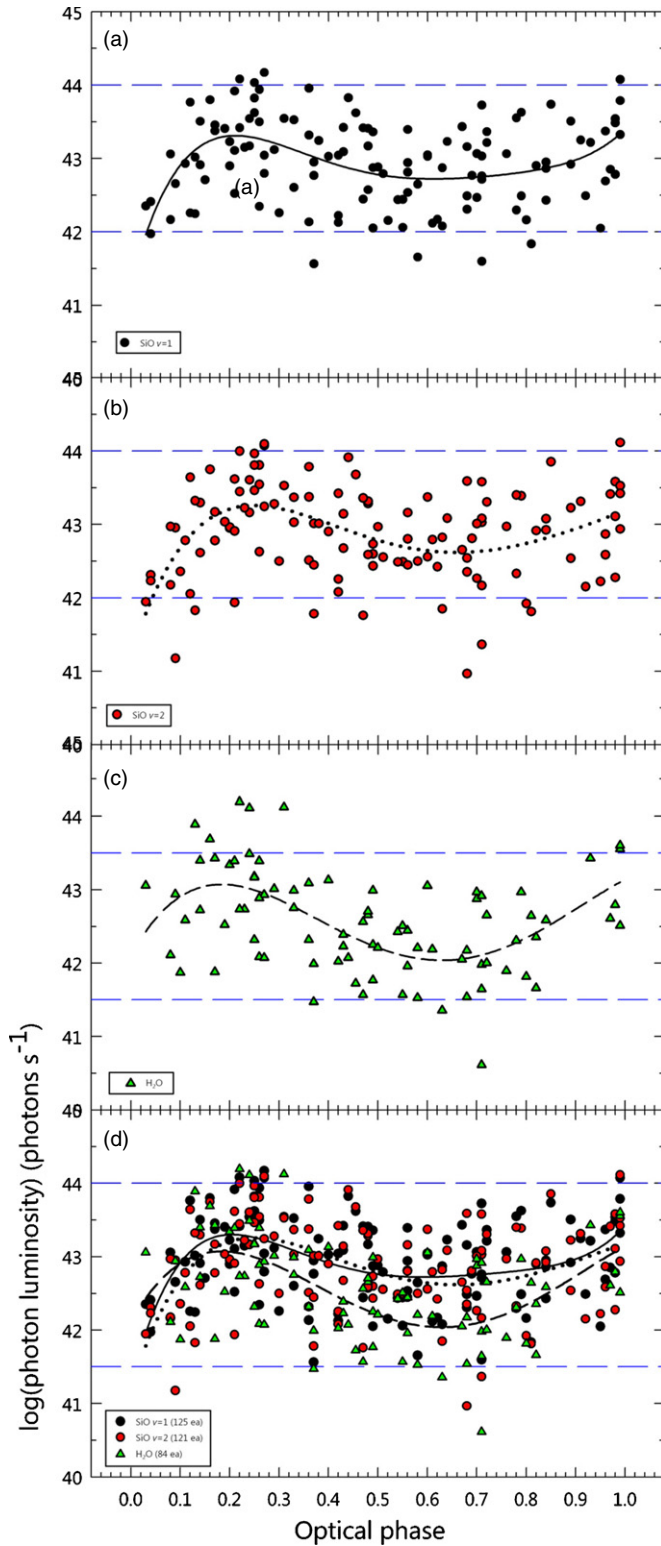


Figure 4. Logarithmic value of SiO $v = 1, 2$ and H₂O photon luminosities according to the optical phase. The solid, dotted, and dashed lines represent the results of the least squares fit, respectively. The symbols used are described in the legend inside the plot. Panel (d) is the overlaid plot of panels (a)–(c).

luminosities of the H₂O maser for 84 stars. The solid, dotted, and dashed lines represent the results of the least squares fit for the photon luminosities of SiO $v = 1, 2$ and H₂O masers, respectively. In Figure 4(d), all of the photon luminosities and fitted lines of both SiO $v = 1, 2$ and H₂O masers are plotted.

In these plots, supergiants were excluded because they usually have higher luminosities – ranging from 10^{44} photons s^{-1} to 10^{46} photons s^{-1} – than Mira variables. For the fitted samples, most photon luminosities of the SiO $v = 1$ and 2 masers are distributed from 10^{42} photons s^{-1} to 10^{44} photons s^{-1} , while photon luminosities of H₂O masers are generally distributed from $10^{41.5}$ photons s^{-1} to $10^{43.5}$ photons s^{-1} .

The maximum photon luminosities of SiO $v = 1$ and 2 masers appear near an optical phase of 0.2, as shown in Figures 4(a) and (b). A similar tendency is shown in the distribution of the photon luminosity of H₂O masers, as shown in Figure 4(c). However, as shown in Figure 4(d), it is remarkable that the photon luminosities of H₂O masers tend to be more dependent on optical phase than those of SiO masers, showing much more photon luminosity variation around the optical minimum. These facts may suggest that the H₂O maser emission is more affected by the stellar pulsation compared with SiO masers. The H₂O maser is explained by only collisional pumping mechanism, unlike the SiO maser. The H₂O masers are excited in the shocked environment by an interaction with the circumstellar thick gas envelope (Cooke & Elitzur 1985). Therefore, the high degree of photon luminosity variation in the H₂O maser around the minimum may be related to the shock waves from the central star. According to Humphreys et al. (2002), shock waves play an important role in SiO maser pumping. Near the photosphere, the shock produces optical emission lines including Balmer hydrogen lines. With growing distance from the photosphere, the shock weakens and the ionization of the gas ceases. The shock then affects the inner layers of the CSE where SiO masers are located. The SiO masers require higher densities and temperatures than H₂O masers. The most suitable conditions may be just behind the shock fronts. According to the model and the interferometric data of H₂O masers, we accept that 22 GHz H₂O masers are localized at the outer parts of the dust formation layer ($\sim 10^{15}$ cm from the central star; Cooke & Elitzur 1985). As the shock reaches the layer, the gas is rapidly heated, whereas dust is controlled by the radiation field of the star and remains cooler than the gas. The H₂O maser is pumped by collisions with particles of the ambient gas in this zone. Here, variations in the mass-loss rate may yield similar effects on the circumstellar gas density and, accordingly, on the maser pumping rate. Therefore, H₂O masers may be more dependent on the optical phase than SiO masers.

The histograms of Figure 5 show the number of stars as a function of the logarithmic photon luminosities of SiO $v = 1$ and H₂O masers for 165 and 99 Mira variables and for 48 and 27 OH/IR stars whose distances have been measured, respectively. The average photon luminosities are indicated as dashed lines. The average value of SiO $v = 1$ photon luminosities of Mira variables is estimated to be $10^{43.1}$ photons s^{-1} and that of the H₂O photon luminosities is $10^{42.8}$ photons s^{-1} , while the average value of SiO $v = 1$ photon luminosities of OH/IR stars is estimated to be $10^{43.4}$ photons s^{-1} and that of the H₂O photon luminosities is $10^{43.2}$ photons s^{-1} . These values of SiO luminosities are very similar to the values derived by Lépine et al. (1978) and Cho et al. (1996). Moreover, the average value of H₂O luminosities is also similar to the value derived by Bowers & Hagen (1984). These values indicate that, on average, the SiO photon luminosity is higher than that of H₂O for both Mira variables and OH/IR stars and the photon luminosities of OH/IR stars are higher than those of Mira variables. Studying a sample of H₂O maser sources, including Mira variables, OH/IR stars, and M supergiants, Bowers & Hagen (1984)

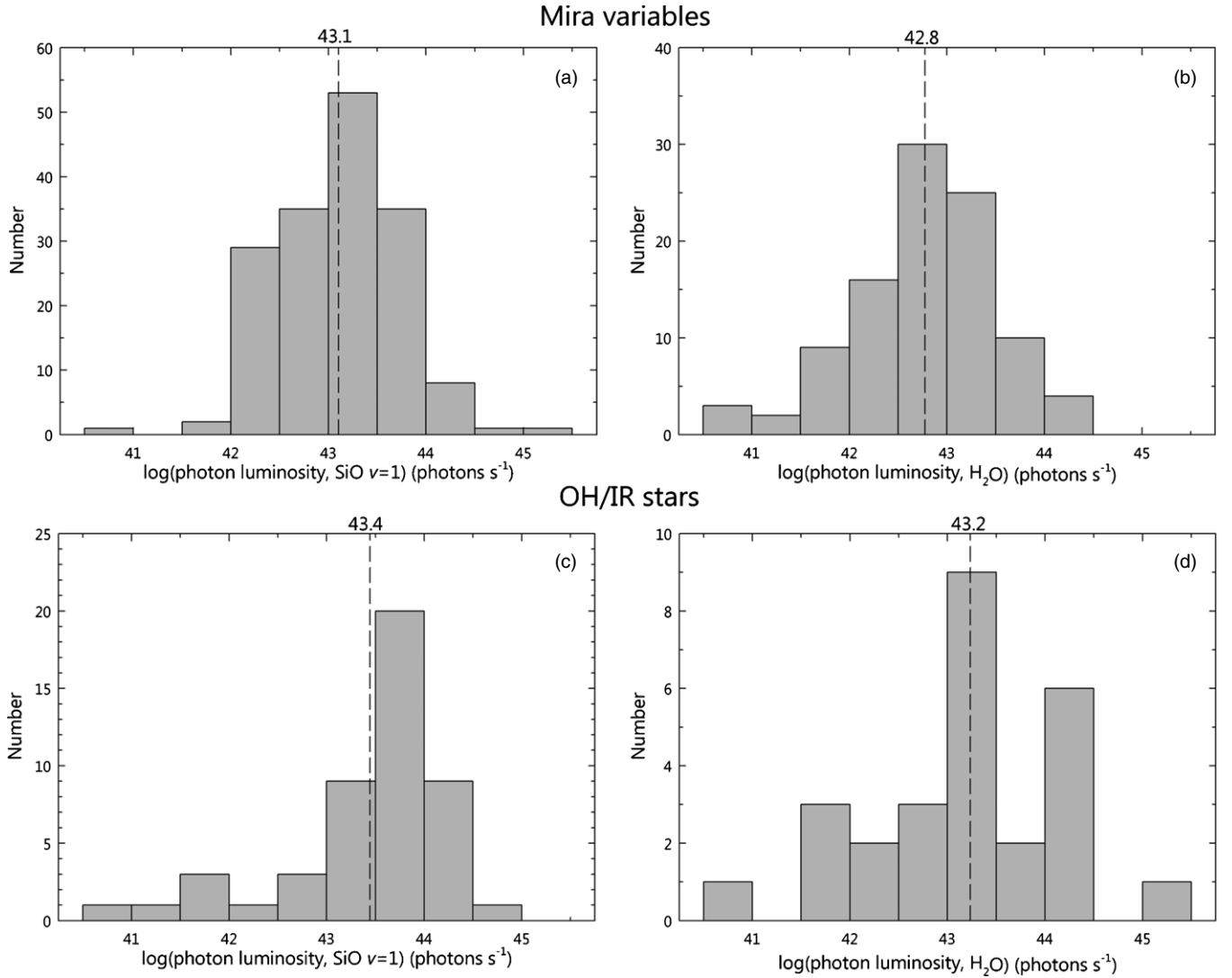


Figure 5. Logarithmic distributions of SiO $v = 1$ and H₂O photon luminosities for Mira variables ((a) and (b)) and OH/IR stars ((c) and (d)). The dashed line represents the average value of the logarithmic photon luminosities.

found that the H₂O luminosities are correlated with mass-loss rate. Therefore, it is reasonable that the H₂O luminosities of OH/IR stars are higher than those of Mira variables because it is generally known that OH/IR stars are more evolved than Mira variables and have higher mass-loss rates. Also, the higher SiO luminosities than those of H₂O masers for both Mira variables and OH/IR stars may be associated with the fact that SiO maser emission is emitted from higher temperature and density regions than H₂O maser emission.

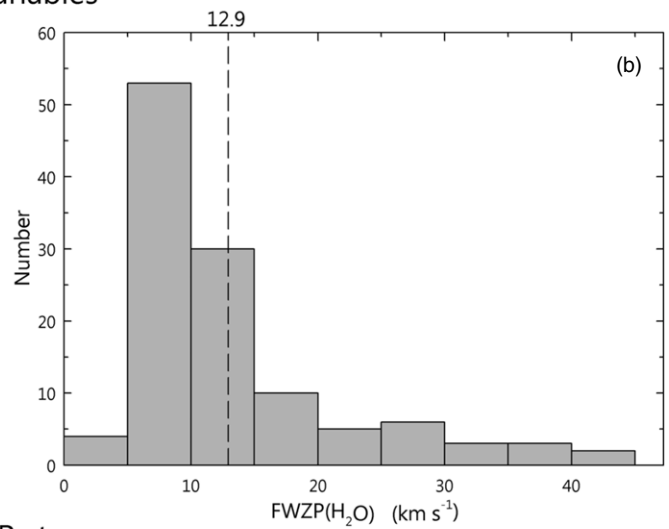
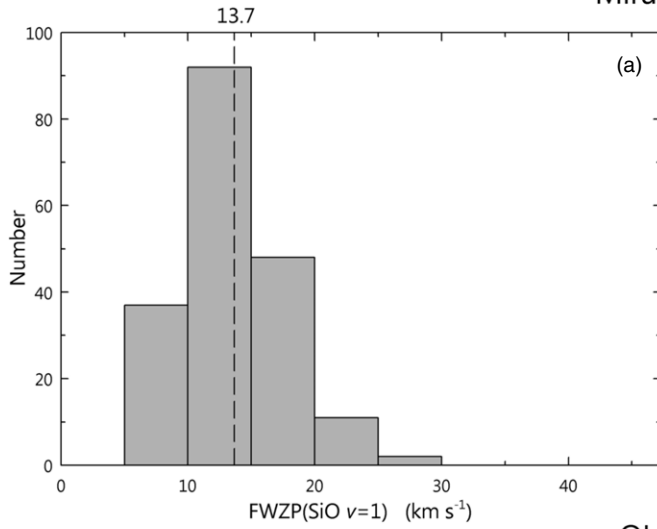
3.3. Full Width at Zero Power of SiO and H₂O Masers

In order to investigate the outflow velocity of masers according to the evolutionary stages of Mira variables and OH/IR stars, we measured FWZPs. The observations require high sensitivity to accurately determine the full width of SiO and H₂O velocity ranges. However, we can identify the general trend through a statistical treatment of a large number of sources within our rms noise levels.

The distribution of the FWZPs of SiO $v = 1$ and H₂O maser lines for Mira variables and OH/IR stars are presented as a histogram in Figure 6. The average values of the FWZPs are indicated as dashed lines. For Mira variables, the velocity extent

of the SiO $v = 1$ and H₂O masers are 5.4–26.6 km s⁻¹ and 3.9–43.3 km s⁻¹, respectively. On the other hand, for OH/IR stars, the velocity extent of the SiO $v = 1$ and H₂O masers are 3.5–30.1 km s⁻¹ and 7.0–49.8 km s⁻¹, respectively. For Mira variables, the average FWZP of SiO $v = 1$ masers is estimated to be 13.7 km s⁻¹ and that of H₂O masers is 12.9 km s⁻¹, while for OH/IR stars, the average FWZP of SiO $v = 1$ masers is estimated to be 13.3 km s⁻¹ and that of H₂O masers is 25.5 km s⁻¹. As a whole, the velocity extents and average FWZPs of SiO masers show a similar range and value for both Mira variables and OH/IR stars, while the values of H₂O masers of OH/IR stars show a large value compared with those of Mira variables. In Figure 7, we distributed the number of sources as a function of the FWZP ratios of the H₂O to SiO $v = 1$ maser lines for Mira variables (1) and OH/IR stars (2), respectively. Their ratio percentages are also indicated in Figure 7. The FWZPs of H₂O masers are narrower than those of SiO masers for most of the Mira variables (FWZP(H₂O)/FWZP(SiO $v = 1$) < 1:69%), while they are broader than those of SiO masers for most of the OH/IR stars (FWZP(H₂O)/FWZP(SiO $v = 1$) ≥ 1:69%). The average ratios of the FWZPs of H₂O masers relative to those of SiO are 0.98 for Mira variables and 2.14

Mira variables



OH/IR stars

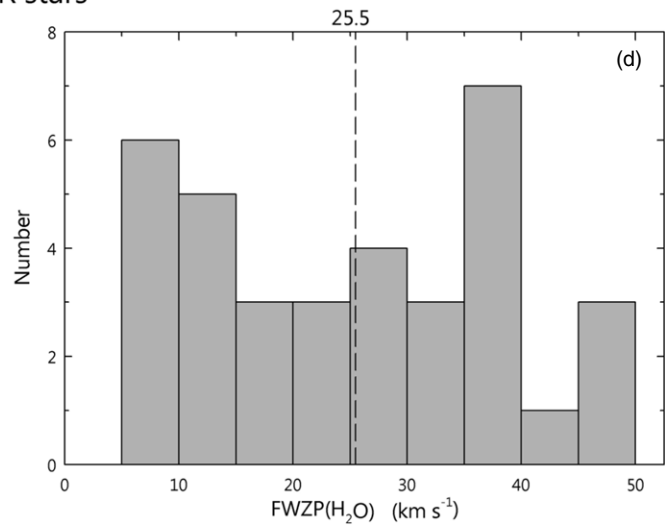
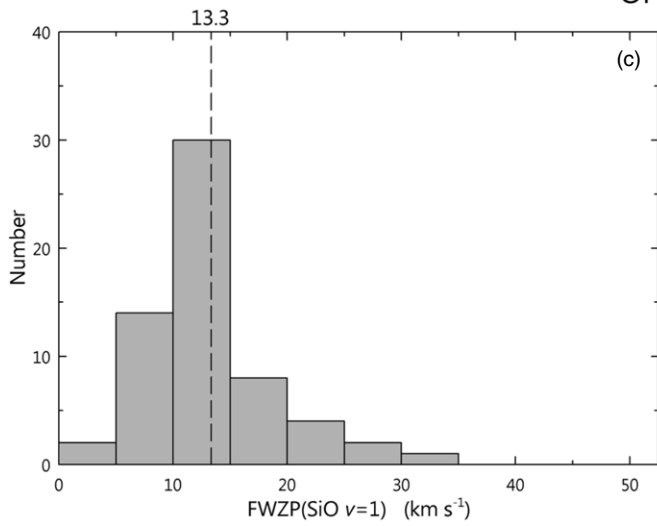


Figure 6. Number of sources as a function of the FWZP of the SiO $v = 1$ and H₂O maser lines for Mira variables ((a) and (b)) and OH/IR stars ((c) and (d)). The dashed line represents the average value of the FWZPs.

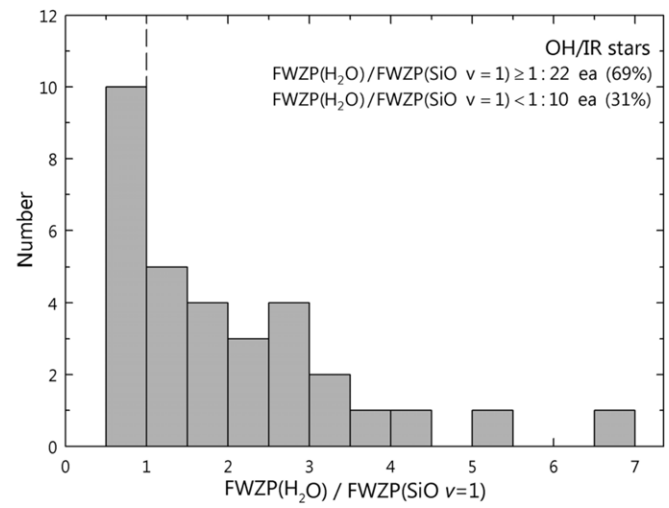
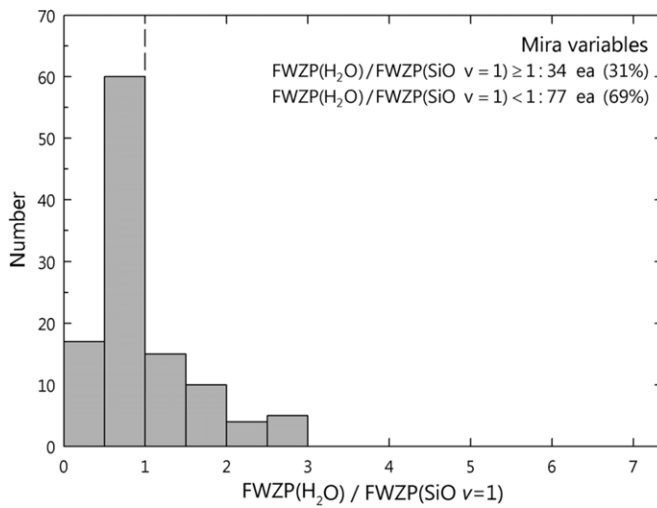


Figure 7. Number of sources as a function of the FWZP ratios of the H₂O to SiO $v = 1$ maser lines for Mira variables (a) and OH/IR stars (b).

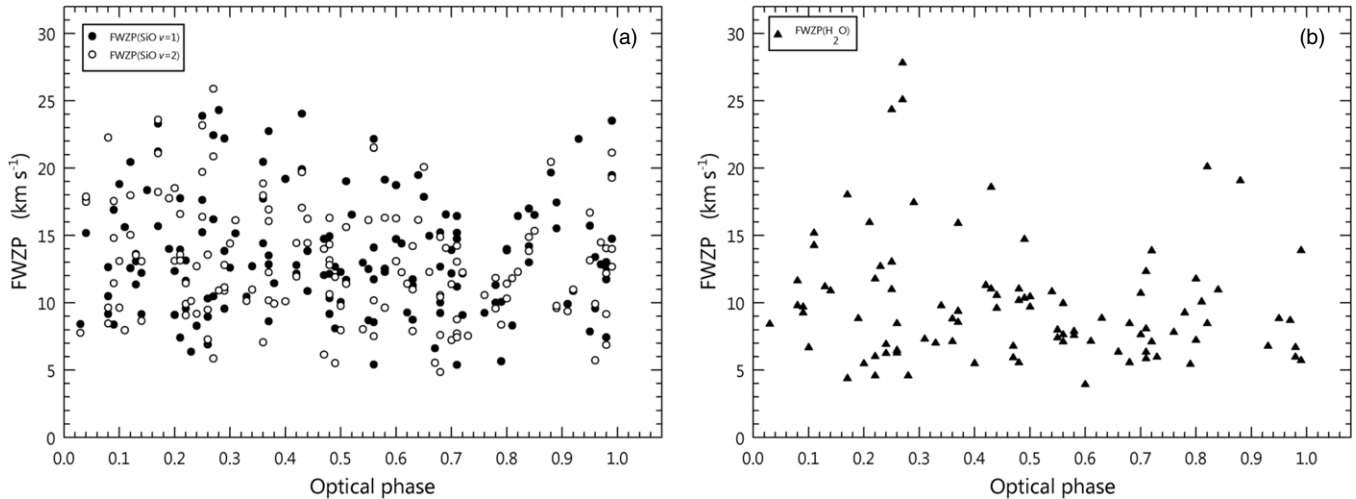


Figure 8. FWZPs of the (a) SiO $v = 1, 2$ and (b) H₂O maser lines according to the optical phase. The symbols used are described in the legend inside the plot.

for OH/IR stars. These differences between Mira variables and OH/IR stars may originate from the different mass-loss rates connected with different expansion velocities. The OH/IR stars show higher mass-loss rates with more extended envelopes than Mira variables (Benson & Little-Marenin 1996).

The 22 GHz H₂O masers come from above the dust-forming layers and they can trace the expansion velocity connected to the mass-loss rates. The SiO masers occur inside dust-forming layers where expansion and infall motions coexist and are influenced by the stellar pulsation directly (Diamond et al. 1994; Diamond & Kemball 2003). Thus, FWZPs of H₂O masers show a large value in OH/IR stars, which show higher mass-loss rates than Mira variables.

In Figure 8, we plot the FWZPs of the SiO $v = 1, 2$ and H₂O maser lines with respect to the optical phase from Table 3. The FWZPs of H₂O maser lines show a large value around the optical maxima, 0.2–0.3, compared with other phases. The FWZPs of SiO $v = 1$ and 2 lines also show a similar trend. However, it seems that the FWZPs of SiO masers are less dependent upon the optical phases than those of H₂O masers.

3.4. Velocity Patterns of SiO and H₂O Masers

Humphreys et al. (2002) suggested that pulsation-driven shock waves propagate out from the central star through the masing region, affecting the velocity of maser lines. Therefore, in order to investigate the dynamic effect of shock waves on SiO and H₂O maser emission, we examined the mean velocity patterns of both the SiO and H₂O maser lines with respect to stellar velocities according to optical phases. In Figures 9(a)–(c), we plot the velocity shifts of the mean velocities of the SiO $v = 1, 2$ and H₂O masers with respect to stellar velocities according to optical phases, as Cho et al. (1996) did. Hinkle et al. (1984, 1997) provide direct observational evidence for shock waves. For several Mira variables and semi-regular variables, they measured large variations of radial velocity amplitude (20–30 km s⁻¹) that are dependent upon optical phase. These phase-dependent radial velocity patterns were measured according to pulsation in CO $\Delta V = 3$ (1.6 μm), which originated from an atmosphere close to a central star. For comparison with the velocity shifts of SiO and H₂O masers, the CO $\Delta V = 3$ (1.6 μm) velocity curve for R Cas, an example of representative sample data, is also presented in Figure 9(d). The velocity curve of this line intersects at the mean stellar phase

of 0.38 ± 0.05 while being blueshifted below a phase of ~ 0.38 and redshifted above (Hinkle et al. 1997). The double line (both blueshifted and redshifted) phases appear in the range 0–0.2 and 0.9–1.2 due to the infall gas of the pulsation.

In Figure 9(c), for the H₂O maser sources, the sources with redshifted emission, i.e., with a positive value of [mean velocity – stellar velocity], are dominant during the phases from 0.3–0.6, while the sources with blueshifted emission coexist with those of redshifted emission during all other phases. A similar tendency is also seen in the SiO $v = 2$ maser sources, in which the redshifted emission is more or less concentrated during the phases from 0.30–0.67, as shown in Figure 9(b). However, the velocity shifts of H₂O maser sources are more dependent on optical phase than are those of SiO $v = 2$ sources. In the case of the SiO $v = 1$ maser sources, it is difficult to reproduce the above association between the velocity shift and the optical phase, as shown in Figure 9(a). From the velocity pattern of H₂O maser sources, 22 GHz H₂O maser emission also seems to be affected by stellar pulsation, as Imai et al. (2003) already suggested. However, the velocity shifts in Figure 9 are not monitoring the results of individual sources but are instead combinations of many sources in various optical phases. Therefore, we need simultaneous time monitoring observations of SiO and H₂O masers toward individual stars in which optical phases are obviously identified.

The histogram of Figure 10 displays the distribution of sources as a function of the velocity differences between the mean velocity and the stellar velocity for 305 sources of SiO $v = 1$ masers, 300 sources of SiO $v = 2$ masers, and 216 sources of H₂O masers, respectively. As shown in Figures 10(a) and (b), for SiO $v = 1$ and 2 masers, the number of redshifted sources is larger than that of blueshifted sources (139 blueshifted and 166 redshifted sources for $v = 1$ and 121 blueshifted and 179 redshifted sources for $v = 2$), whereas, for H₂O masers, the number of blueshifted sources is larger than that of redshifted sources (110 blueshifted and 106 redshifted sources), as shown in Figure 10(c). The average velocity shifts of SiO $v = 1$ and 2 maser sources are estimated to be 0.4 km s⁻¹ and 0.6 km s⁻¹, respectively, while that of the H₂O maser sources is estimated to be -0.5 km s⁻¹. This trend of H₂O maser emission was found from OH/IR stars by Engels et al. (1986) and Engels & Lewis (1996) and from semi-regular variables by Wallerstein & Dominy (1988) and Szymczak & Engels (1995).

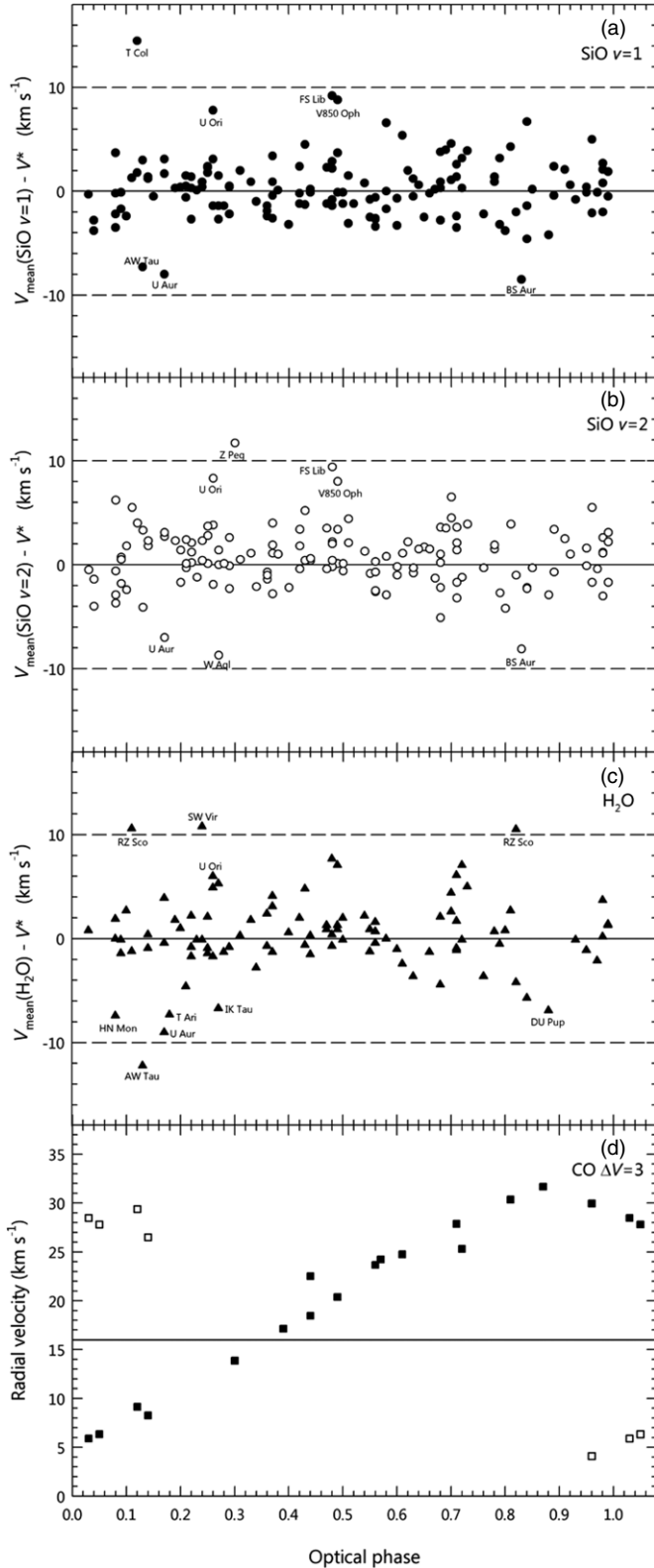


Figure 9. (a)–(c) Velocity shift between the mean velocity and the stellar velocity ($V_{\text{mean}} - V^*$) for SiO $v = 1$ (filled circle), 2 (open circle), and H₂O (filled triangle) masers according to the optical phase. The solid line corresponds to an equal value between the mean velocity and the stellar velocity. The relatively highly redshifted or blueshifted stars are marked. (d) CO, $\Delta V = 3$ ($1.6 \mu\text{m}$) radial velocity curve for R Cas from Hinkle et al. (1984). Filled squares show the evolution during a light cycle. Open squares repeat the data backward and forward in time. The solid line represents the systemic velocity derived from thermal SiO and CO transitions.

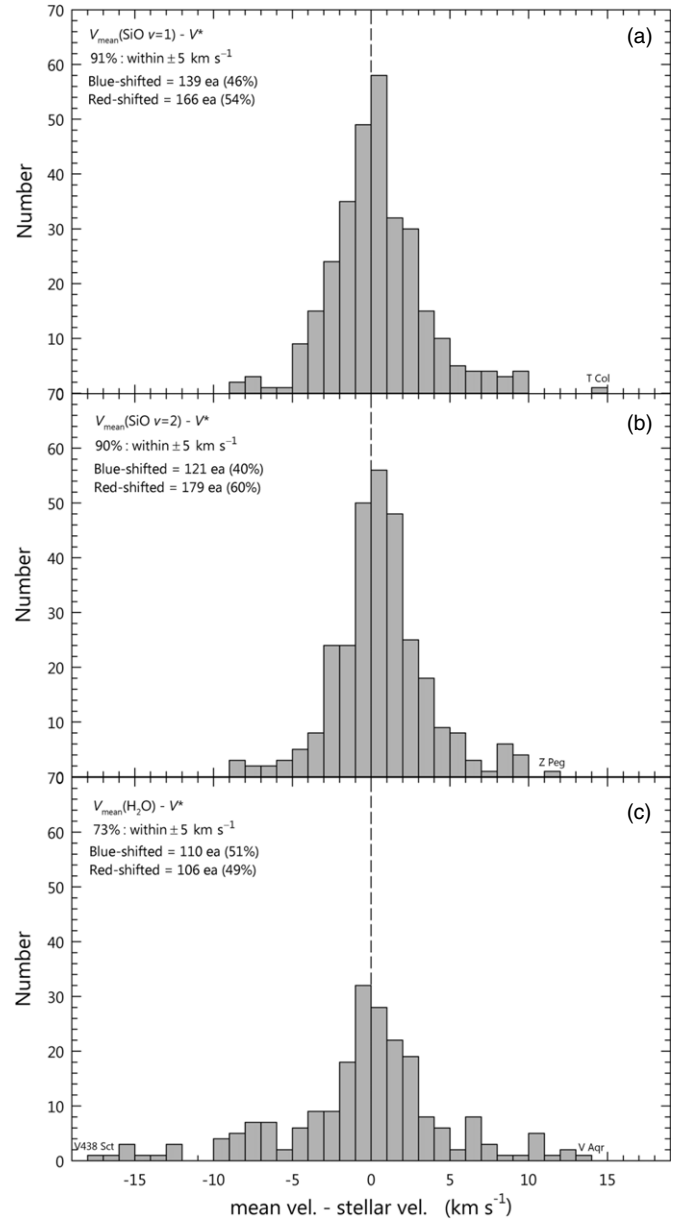


Figure 10. Histogram of the velocity shift between the mean velocity and the stellar velocity ($V_{\text{mean}} - V^*$) for SiO $v = 1, 2$ and H₂O masers.

They considered that the blueshifted H₂O emission is a general characteristic of an emission line occurring from circumstellar shells. Cho et al. (1996) reported that the redshifted emission is dominant in the vibrationally excited SiO masers ($v = 1, 2, 3$, $J = 1-0$). Most mean velocities of SiO $v = 1$ and 2 masers (91% for $v = 1$ and 90% for $v = 2$) are distributed within $\pm 5 \text{ km s}^{-1}$ with respect to the stellar velocities, while 73% of H₂O maser mean velocities are distributed within $\pm 5 \text{ km s}^{-1}$. This result also implies that SiO masers arise from close to the central star and, in contrast, H₂O masers occur above dust layers and are sensitive to outflow motions.

3.5. IRAS Two-color Diagram of All Observed Stars

The IRAS two-color diagram (van der Veen & Habing 1988) has proved to be an efficient tool for the discussion of the properties and evolutionary status of AGB stars. Mira variables, OH/IR stars, and protoplanetary nebulae (PPNe) occupy different regions in the diagram due to the different

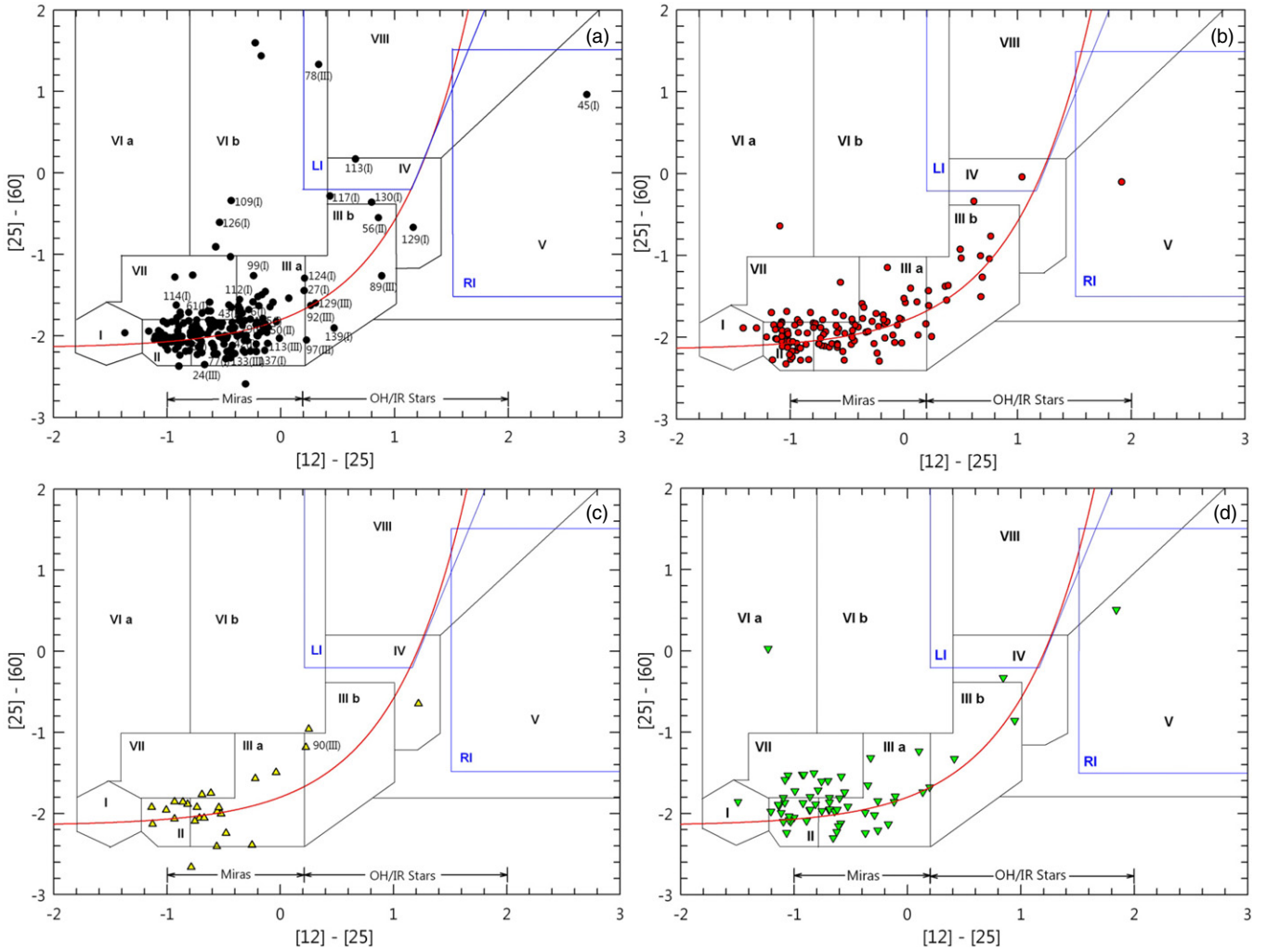


Figure 11. *IRAS* two-color diagrams according to the detected maser. (a) The black circles indicate both SiO and H₂O maser detected sources. (b) The red circles indicate the SiO-only detected sources. (c) The yellow triangles indicate the H₂O-only detected sources. (d) Both SiO and H₂O maser undetected sources are marked with green inverted triangles. The sources with one-way, double, and multiple peaks of the H₂O maser are identified by their identification numbers from Table 2.

properties of their dust shells, although there is overlap. Moreover, the position of a source in the *IRAS* two-color diagram partly reflects its mass-loss history. Figure 11 shows an *IRAS* two-color diagram for all of our 401 observed sample sources using the *IRAS* Point Source Catalog v2.1 (<http://irsa.ipac.caltech.edu/cgi-bin/Gator/nph-dd>). To investigate the characteristics of the detected masers, we divided the sources into detected maser classes: both SiO and H₂O detected, SiO-only detected, H₂O-only detected, and both undetected. The *IRAS* colors are defined as $[12]-[25] = 2.5 \log (S_{25}/S_{12})$ and $[25]-[60] = 2.5 \log (S_{60}/S_{25})$, respectively. The observational results are designated by different symbols. Black circles denote that both SiO and H₂O maser emission was detected (Figure 11(a)) and red circles and yellow triangles indicate SiO-only detected sources without H₂O maser detections and H₂O-only detected sources without SiO maser detections, respectively (Figures 11(b) and (c)). Both undetected sources are marked with green inverted triangles (Figure 11(d)). The red line represents the evolutionary track for AGB stars defined by van der Veen & Habing (1988).

Most of our observed stars are mainly distributed in Regions II and IIIa. The Region IIIb stars consist of variable stars with thick O-rich circumstellar shells. The “LI” (Left of *IRAS*) and “RI” (Right of *IRAS*) regions, designated by blue lined areas,

are associated with post-AGB stars, as suggested by Sevenster (2002). The SiO-only detected sources (red circles) appear in a wide range of color indices, as shown in Figure 11(b), while the H₂O-only detected sources are distributed in Region II and the front part of Region IIIa, except five sources. In other words, the H₂O maser emission in our observed AGB star samples occurs at an earlier evolutionary stage of AGB stars compared with SiO masers. Namely, there is no H₂O-only maser detected sources in Region IIIb except one source that is located on the border between Regions IIIa and IIIb. This source, No. 90(III). IRAS 19075+0921, is classified as a PPN candidate by Meixner et al. (1999) and Kohoutek (2001) and is also assigned as a carbon star by Alksnis et al. (2001). This source was described in Section 3 of Paper III as an individual source.

We already discussed the lack of H₂O maser detection in Region IIIb in Paper I. Furthermore, Engels (2002) suggested that a very early phase of PPNe (or a very late stage of the AGB stars) are thought to have stopped their pulsations and the associated strong mass loss and a hollow shell has therefore developed and continues to expand. The densities of objects with hollow shell interiors will have dropped sharply. Engels suggested, therefore, that this absence of H₂O maser was due to the expected drop in the densities in the H₂O maser zone, after which the inner boundary of the hollow shell passed.

We examined the distribution of the sources with one-way, double, and multiple peaks of H₂O maser lines in the *IRAS* two-color diagram (Figure 11). These one-way, double, and multiple peaks of H₂O maser lines can be associated with an asymmetric wind and bipolar outflows, which are commonly seen in PPNe and PNe. Therefore, the search for these H₂O maser spectra would be one method for identifying very young PPN candidates, as suggested by Lewis (1989) and Engels (2002). These one-way and double peak sources, which are marked with identification numbers, are mainly distributed in Regions IIIb, IV, V, and VIb with a relatively high percentage of one-way and double-peak lines compared with those of Region II, IIIa, and VII stars. This tendency was already noted in Paper I. These types of H₂O maser sources increased from 24 (Figure 2 of Paper I) to 42 sources, as shown in Figure 11(a). In particular, No. 45(I), QX Pup, No. 78(III), OH24.7–0.1, and No. 113(I), OH 24.7+0.2 are located in LI and RI regions, respectively. No. 45(I), QX Pup is a well-known bipolar PPN (Desmurs et al. 2007) but No. 113(I), OH24.7+0.2 is not identified as a bipolar PPN, as discussed in Paper I. No. 78(III), OH24.7–0.1 is also not identified as a bipolar PPN. Nevertheless, OH24.7–0.1 has certain one-way and blueshifted triple peaks of H₂O maser emission relative to the stellar velocity and has a large H₂O velocity extent of 49.4 km s⁻¹. OH24.7+0.2 has an H₂O line profile characteristic of double peaks and its velocity extent is about 45.1 km s⁻¹. These two sources are thought to be PPN candidates. Moreover, in Region IV, No. 117(I), V438 Sct has a highly blueshifted one-way peak of H₂O maser emission with a velocity extent of 43.3 km s⁻¹ and No. 130(I), IRAS 19069+0916 has a double peaked H₂O emission with a strong blueshifted peak component. The velocity extent of IRAS 19069+0916 is about 48.0 km s⁻¹. However, PPN candidates are not restricted to these areas (Volk 1992; van Hoof et al. 1997). By all accounts of Papers I–III, candidates for young PPNe can be also distributed in Region IIIb. Out of nine H₂O detections in Region IIIb, eight show one-way or double peaks in their H₂O maser lines, although the total number of observed sources is limited. Most of these sources have H₂O velocity extents of about 30–40 km s⁻¹, in which H₂O masers appear near the terminal velocities of OH shells. This tendency implies that the development of asymmetries, including bipolar outflows, is active in the late-stage evolution of AGB stars.

4. SUMMARY

Based on the observational results of Papers I–III, we have established homogeneous observational data for SiO and H₂O maser properties including peak and integrated intensity ratios, photon luminosities, FWZPs and their ratios, and the velocity shifts with respect to stellar velocities for all 401 observed evolved stars. Therefore, we have made a systematic statistical study of the mutual relation between SiO and H₂O maser properties including evolutionary characteristics.

1. In both Mira variables and OH/IR stars, the peak and integrated intensities of SiO masers are stronger than those of H₂O masers and the relative intensity ratios of H₂O to SiO maser in OH/IR stars are larger than those in Mira variables. We have also investigated the dependence of the peak and integrated intensity ratios of H₂O to SiO $v = 1$ masers according to the optical phases. The SiO $v = 1$ masers emit at a stronger intensity than H₂O masers in most optical phases. However, a large percentage

of sources that have stronger H₂O maser intensity than SiO maser intensity are distributed around optical phases ranging from 0–0.4. This means that H₂O maser intensity rapidly increases around these optical maximum phases compared with SiO maser intensity. This tendency seems to be supported by monitoring observations of an individual source, W Hya. In the monitoring of SiO and H₂O masers toward W Hya, the peak intensity of the H₂O maser also rapidly increases around the maximum optical phase.

2. The maximum photon luminosities of SiO $v = 1$ and 2 masers appear near an optical phase of 0.2 and a similar tendency is seen in the distribution of the photon luminosities of H₂O masers. However, it is remarkable that the photon luminosities of H₂O masers tend to be more dependent on the optical phase than are those of SiO masers, showing significant photon luminosity variation around the optical minimum. These facts may suggest that the H₂O maser emission is more affected by the stellar pulsations than SiO masers. We have also identified that the average value of SiO $v = 1$ photon luminosities of Mira variables is estimated to be $10^{43.1}$ and that of the H₂O photon luminosities is $10^{42.8}$, while the average value of SiO $v = 1$ photon luminosities of OH/IR stars is estimated to be $10^{43.4}$ and that of the H₂O photon luminosities is $10^{43.2}$ photons s⁻¹. These values of SiO and H₂O luminosities are similar to previously known values.
3. The average FWZPs (velocity extents) of SiO masers show a similar value in both Mira variables and OH/IR stars, while those of H₂O masers in OH/IR stars are larger than those in Mira variables. These differences between Mira variables and OH/IR stars may originate from the different mass-loss rate and location of the two masers. The 22 GHz H₂O masers arise from above dust-forming layers and trace the expansion velocity connected to the mass-loss rates, while SiO masers occur inside dust-forming layers where gas acceleration and deceleration motions coexist. The OH/IR stars show higher mass-loss rates than Mira variables with more extended CSEs.
4. The mean velocity shifts of SiO and H₂O masers with respect to stellar velocities were investigated as a function of optical phases. H₂O maser sources show dominant redshifted emission between the optical phases 0.3–0.6, while the blueshifted emission appears at a phase of 0.6 and coexists with the redshifted emission during all other phases. These features agree with the CO $\Delta V = 3$ radial velocity curve, which exhibits a typical pulsation motion. On the other hand, the velocity shifts of SiO $v = 2$ masers show slightly similar features compared with those of H₂O masers, while those of SiO $v = 1$ masers do not show such features. These facts may suggest that the intensity of H₂O masers is more sensitive to stellar pulsation than the SiO masers are since H₂O is collisionally pumped. However, we need simultaneous time monitoring observations of H₂O and SiO masers for individual sources.
5. The distributions of all 401 observed sources were investigated in the *IRAS* two-color diagram in relation with late evolutionary stages of AGB stars. Most of our observed stars are distributed in Regions II and IIIa. We confirmed that SiO maser detected sources appear in a wide range of color indices, while H₂O maser-only detected sources are distributed in Region II and the front part of Region IIIa, except for the five sources shown in Papers I–III. We examined the distribution of the sources with one-way and

double peaked H₂O maser lines for all H₂O maser detected sources in the *IRAS* two-color diagram. We also confirmed that the one-way and double peak sources are distributed in Regions IIIb, IV, V, and VIb with a relatively high percentage compared with those of Regions II, IIIa, and VII stars. This tendency implies that a development of asymmetry and bipolar outflows in a CSE is active at the late-stage evolution of AGB stars.

Finally, simultaneous observations of SiO and 22 GHz H₂O maser emission toward 401 AGB stars and systematic statistical analyses based on these homogeneous data provide good information on combined studies between SiO and H₂O masers in relation to stellar pulsation, together with the stellar evolution of the late AGB stage.

This work was supported by the Leading Research Program (2011–2013) of KASI and was partially supported by “KASI–Yonsei Joint Research Program (2011–2013) for the Frontiers of Astronomy and Space Science.” S.J.K. was supported by a grant from Kyung Hee University in 2013 and thanks the KASI collaboration program between university and government-funded research (2011–2013).

REFERENCES

- Alcolea, J., Pardo, J. R., Bujarrabal, V., et al. 1999, *A&AS*, **139**, 461
 Alksnis, A., Balklavs, A., Dzervitis, U., et al. 2001, *BaltA*, **10**, 1
 Ammons, S. M., Robinson, S. E., Strader, J., et al. 2006, *ApJ*, **638**, 1004
 Anderson, E., & Francis, C. 2012, *AstL*, **38**, 331
 Benson, P. J., & Little-Marenin, I. R. 1990, *BAAS*, **22**, 1208
 Benson, P. J., & Little-Marenin, I. R. 1996, *ApJS*, **106**, 579
 Bowers, P. F., & Hagen, W. 1984, *ApJ*, **285**, 637
 Bowers, P. F., & Johnston, K. J. 1994, *ApJS*, **92**, 189
 Bujarrabal, V., Planesas, P., & del Romero, A. 1987, *A&A*, **175**, 164
 Cho, S.-H., Kaifu, N., & Ukita, N. 1996, *AJ*, **111**, 1987
 Cho, S.-H., & Kim, J. 2012, *AJ*, **144**, 129 (Paper II)
 Choi, Y. K., Hirota, T., Honma, M., et al. 2008, *PASJ*, **60**, 1007
 Cooke, B., & Elitzur, M. 1985, *ApJ*, **295**, 175
 Deguchi, S., Fujii, T., Glass, I., et al. 2004, *PASJ*, **56**, 765
 Deguchi, S., Sakamoto, T., & Hasegawa, T. 2012, *PASJ*, **64**, 4
 Desmurs, J.-F., Alcolea, J., Bujarrabal, V., Contreras, C. S., & Colomer, F. 2007, *A&A*, **468**, 189
 Diamond, P. J., & Kemball, A. J. 2003, *ApJ*, **599**, 1372
 Diamond, P. J., Kemball, A. J., Junor, W., et al. 1994, *ApJL*, **430**, L61
 Engels, D. 1979, *A&AS*, **36**, 337
 Engels, D. 2002, *A&A*, **388**, 252
 Engels, D., & Lewis, B. M. 1996, *A&AS*, **116**, 117
 Engels, D., Schmid-Burgk, J., & Walmsley, C. M. 1986, *A&A*, **167**, 129
 Gonidakis, I., Diamond, P. J., & Kemball, A. J. 2010, *MNRAS*, **406**, 395
 Hale, D. D. S., Bester, M., Danchi, W. C., et al. 1997, *ApJ*, **490**, 407
 Hinkle, K. H., Lebzelter, T., & Scharlach, W. W. G. 1997, *AJ*, **114**, 2686
 Hinkle, K. H., Scharlach, W. W. G., & Hall, D. N. B. 1984, *ApJS*, **56**, 1
 Humphreys, E. M. L., Gray, M. D., Yates, J. A., et al. 2002, *A&A*, **386**, 256
 Imai, H., Sahai, R., & Morris, M. 2007, *ApJ*, **669**, 424
 Imai, H., Shibata, K. M., Marvel, K. B., et al. 2003, *ApJ*, **590**, 460
 Ita, Y., Deguchi, S., Fujii, T., et al. 2001, *A&A*, **376**, 112
 Izumiura, H., Deguchi, S., Hashimoto, O., et al. 1995, *ApJ*, **453**, 837
 Jewell, P. R., Snyder, L. E., Walmsley, C. M., Wilson, T. L., & Gensheimer, P. D. 1991, *A&A*, **242**, 211
 Jura, M., & Kleinmann, S. G. 1989, *ApJ*, **341**, 359
 Justanont, K., Olofsson, G., Dijkstra, C., & Meyer, A. W. 2006, *A&A*, **450**, 1051
 Kastner, J. H., Weintraub, D. A., Zuckerman, B., et al. 1992, *ApJ*, **398**, 552
 Kim, J., Cho, S.-H., & Kim, S. J. 2013, *AJ*, **145**, 22 (Paper III)
 Kim, J., Cho, S.-H., Oh, C. S., & Byun, D.-Y. 2010, *ApJS*, **188**, 209 (Paper I)
 Kohoutek, L. 2001, *A&A*, **378**, 843
 Le Bertre, T., Tanaka, M., Yamamura, I., & Murakami, H. 2003, *A&A*, **403**, 943
 Lekht, E. E., Rudnitskij, G. M., Mendoza-Torres, J. E., & Tolmachev, A. M. 2005, *A&A*, **437**, 127
 Lépine, J. R. D., Le Squeren, A. M., & Scalise, E., Jr. 1978, *ApJ*, **225**, 869
 Lewis, B. M. 1989, *ApJ*, **338**, 234
 Little-Marenin, I. R., & Benson, P. J. 1991, in *ASP Conf. Ser. 16, Atoms, Ions, and Molecules: New Results in Spectral Line Astrophysics*, ed. A. D. Haschick & P. T. P. Ho (San Francisco, CA: ASP), **73**
 Loup, C., Forveille, T., Omont, A., & Paul, J. F. 1993, *A&AS*, **99**, 291
 Martínez, A., Bujarrabal, V., & Alcolea, J. 1988, *A&AS*, **74**, 273
 McIntosh, G. C. 2006, *AJ*, **132**, 1046
 Meixner, M., Ueta, T., Dayal, A., et al. 1999, *ApJS*, **122**, 221
 Morris, M., & Jura, M. 1983, *ApJ*, **267**, 179
 Nakashima, J., & Deguchi, S. 2003a, *PASJ*, **55**, 203
 Nakashima, J., & Deguchi, S. 2003b, *PASJ*, **55**, 229
 Nakashima, J., & Deguchi, S. 2007, *ApJ*, **669**, 446
 Nakashima, J., Jiang, B. W., Deguchi, S., Sadakane, K., & Nakada, Y. 2000, *PASJ*, **52**, 275
 Nyman, L.-Å., Hall, P. J., & Le Bertre, T. 1993, *A&A*, **280**, 551
 Olivier, E. A., Whitelock, P., & Marang, F. 2001, *MNRAS*, **326**, 490
 Palagi, F., Cesaroni, R., Comoretto, G., Felli, M., & Natale, V. 1993, *A&AS*, **101**, 153
 Pardo, J. R., Alcolea, J., Bujarrabal, V., et al. 2004, *A&A*, **424**, 145
 Pickles, A., & Depagne, E. 2010, *PASP*, **122**, 1437
 Pojmanski, G. 2002, *AcA*, **52**, 397
 Reid, M. J., & Moran, J. M. 1981, *ARA&A*, **19**, 231
 Rudnitskij, G. M., Lekht, E. E., & Berulis, I. I. 1999, *AstL*, **25**, 398
 Sevenster, M. N. 2002, *AJ*, **123**, 2788
 Shintani, M., Imai, H., Ando, K., et al. 2008, *PASJ*, **60**, 1077
 Spencer, J. H., Winnberg, A., Olsson, F. M., et al. 1981, *AJ*, **86**, 392
 Szymczak, M., & Engels, D. 1995, *A&A*, **296**, 727
 van Belle, G. T., Dyck, H. M., Benson, J. A., & Lacasse, M. G. 1996, *AJ*, **112**, 2147
 van Belle, G. T., Thompson, R. R., & Creech-Eakman, M. J. 2002, *AJ*, **124**, 1706
 van der Veen, W. E. C. J., & Habing, H. J. 1988, *A&A*, **194**, 125
 van Hoof, P. A. M., Oudmaijer, R. D., & Waters, L. B. F. M. 1997, *MNRAS*, **289**, 371
 Vassiliadis, E., & Wood, P. R. 1993, *ApJ*, **413**, 641
 Volk, K. 1992, *ApJS*, **80**, 347
 Wallerstein, G., & Dominy, J. F. 1988, *ApJ*, **326**, 292
 Whitelock, P. A., Feast, M. W., & van Leeuwen, F. 2008, *MNRAS*, **386**, 313
 Yi, J., Booth, R. S., Conway, J. E., & Diamond, P. J. 2005, *A&A*, **432**, 531